

Stability analysis of open-channel flows with secondary currents

Original

Stability analysis of open-channel flows with secondary currents / Camporeale, CARLO VINCENZO; Cannamela, Fabio; Canuto, Claudio; Manes, Costantino. - In: JOURNAL OF FLUID MECHANICS. - ISSN 0022-1120. - STAMPA. - 927:(2021). [10.1017/jfm.2021.769]

Availability:

This version is available at: 11583/2928086 since: 2021-09-29T15:00:20Z

Publisher:

Cambridge University Press

Published

DOI:10.1017/jfm.2021.769

Terms of use:

This article is made available under terms and conditions as specified in the corresponding bibliographic description in the repository

Publisher copyright

Cambridge University Press postprint/Author's Accepted Manuscript con licenza CC

This article has been published in a revised form in [Journal] [<http://doi.org/XXX>]. This version is published under a Creative Commons CC-BY-NC-ND. No commercial re-distribution or re-use allowed. Derivative works cannot be distributed. © copyright holder.

(Article begins on next page)

Stability analysis of open channel flows with secondary currents

Carlo Camporeale^{1†}, Fabio Cannamela¹, Claudio Canuto² and Costantino Manes¹

¹Politecnico di Torino, Department of Environment, Land and Infrastructure Engineering, Torino, Italy

²Politecnico di Torino, Department of Mathematical Sciences, Torino, Italy

(Received xx; revised xx; accepted xx)

This paper presents some results coming from a linear stability analysis of turbulent depth-averaged Open Channel Flows (OCFs) with secondary currents. The aim was to identify plausible mechanisms underpinning the formation of large-scale turbulence structures, which are commonly referred to as Large-Scale Motions (LSMs) and Very-Large-Scale-Motions (VLSMs). Results indicate that the investigated flows are subjected to a sinuous instability whose longitudinal wavelength compares very well with that pertaining to LSMs. In contrast, no unstable modes at wavelengths comparable to those associated with VLSMs could be found. This suggests that VLSMs in OCFs are triggered by non-linear mechanisms to which the present analysis is obviously blind. We demonstrate that the existence of the sinuous instability requires two necessary conditions: (i) the circulation of the secondary currents ω must be greater than a critical value ω_c ; (ii) the presence of a dynamically responding free surface (i.e. when the free surface is modelled as a frictionless flat surface, no instabilities are detected). The present paper draws some ideas from the work by Cossu, Hwang and co-workers on other wall flows (i.e. turbulent boundary layers, pipe, channel and Couette flow) and somewhat supports their idea that LSMs and VLSMs might be governed by an outer layer cycle also in OCFs. However, the presence of steady secondary flows makes the procedure adopted herein much simpler than that used by these authors.

Key words: Large Scale Motions; Secondary currents; Open channel flows; Stability analysis.

1. Introduction

Since the seminal work by Kim & Adrian (1999), large scale coherent structures in wall-flows have been broadly classified and referred to as Large Scale Motions (LSMs) and Very Large Scale Motions (VLSMs). There is now wide consensus about the fact that LSMs typically occur as structures with a longitudinal wavelength of a few outer lengths of the flow δ (typically $2-3\delta$), whereas VLSMs have a wavelength of about 10δ and more (Marusic *et al.* 2010). Much less consensus has been reached with respect to the mechanism underpinning the formation of LSMs and VLSMs, which is still elusive and the subject of an ongoing debate. Within this context, two plausible mechanisms are proposed in the literature and are briefly summarized as follows.

† Email address for correspondence: carlo.camporeale@polito.it

Adrian and co-workers support the idea that wall turbulence is dictated by the existence of an omega shaped ‘building-block’ eddy-structure, which is often referred to as *hairpin eddy*. According to Adrian’s view, hairpins can undergo an auto-generation mechanism leading to the formation of packets, which can be interpreted as LSMs. A less clear picture is provided for the generation mechanism of VLSMs, for which Adrian has provided a wide range of plausible hypothesis, among which, the preferred one sees VLSMs as a concatenation of LSMs (Adrian 2007).

Cossu, Hwang and co-workers – hereafter referred to as CH – provide a rather different view (for a review, see Cossu & Hwang 2017). In a nutshell, they argue that the existence of LSMs and VLSMs is the result of a so-called outer-layer cycle that is independent of the existence of a ‘building block’ turbulent structure, i.e. hairpins. These authors argue that such an outer-layer cycle shares strong similarities with the well-known *near-wall cycle*, which has been identified since 30 years as the engine behind turbulence in the buffer zone of wall flows (see e.g. Kim *et al.* 1971; Jimenez & Moin 1991; Hamilton *et al.* 1995; Waleffe 1997). As per the near-wall cycle, the proposed outer-layer cycle involves the existence of low and high (longitudinal) momentum streaks associated with the occurrence of elongated vortices with streamwise vorticity. Such low and high momentum streaks are very long and represent the VLSMs. These authors then suggest that VLSMs are subjected to a so-called lift-up mechanism that amplifies their longitudinal vorticity and leads to a sinuous instability (namely a meander-like amplification of the vortex lines) having a characteristic wavelength comparable to that of LSMs. This instability then leads to a series of non-linear interactions that, eventually, promotes the formation of new longitudinal streaks to re-start the cycle.

It should be noted that the two pictures described above have been developed mainly from the study of (flat plate) turbulent boundary layers, channel flows and pipe flows. Turbulence research in Open Channel Flows (OCF), which is the subject of the present paper, developed somewhat independently, with the consequence that the LSM-VLSM paradigm was introduced only recently to interpret the scaling and dynamics of large-scale turbulence. This does not mean that LSMs and VLSMs have never been detected in OCFs. In fact, structures similar to LSMs and VLSMs have been identified and studied (e.g. Rashidi & Banerjee 1988; Nezu & Nakagawa 1993; Tamburrino & Gulliver 2010; Shvidchenko & Pender 2001; Roy *et al.* 2004; Hurther *et al.* 2007; Bagherimiyab & Lemmin 2018), but they were called differently and never put into any relation with the structures observed in other wall-flows. Perhaps, Adrian & Marusic (2012) were the first to do so, but it was only until the work by Cameron *et al.* (2017); Zhang *et al.* (2019); Duan *et al.* (2020); Peruzzi *et al.* (2020); Duan *et al.* (2021), that the LSM-VLSM dichotomy was really established in OCF research. These papers were the first to classify large-scale structures by means of spectral analysis of long duration measurements of the longitudinal velocity (as per other wall flows) and proved the existence of VLSMs in both hydrodynamically-rough and smooth-bed OCFs.

The works by Cameron *et al.* (2017) and Peruzzi *et al.* (2020) provide strong evidence that LSMs follow roughly the same scaling as reported for other wall flows. In contrast, VLSMs were observed to scale differently because their longitudinal wavelength seems to be dependent on the aspect ratio of the flow (i.e. the ratio between channel width and flow depth). Furthermore, it was observed that VLSMs could be detected through spectral analysis at von Karman numbers $Re_\tau = \delta/\delta_\nu$ rather lower than in other wall-flows (where δ_ν is the viscous length scale). This result is worthwhile as it puts OCFs developing in standard laboratory flumes in good similarity with much higher Re_τ flows occurring in nature, which is something that is only achievable with the employment of very large and costly facilities in other wall flows (Marusic *et al.* 2010).

As per other wall flows, the mechanisms leading to the formation of both LSMs and VLSMs in OCFs are not well understood. There seems to be a slight tendency in the OCFs community to interpret the scaling and growth of large-scale structures using the bottom-up paradigm and methods developed by Adrian and co-workers (Adrian & Marusic 2012). The outer layer cycle paradigm developed by CH has instead received less attention. The aim of the present paper is to make a first step into the application of such a paradigm to explain the scaling and dynamics of large-scale turbulence in OCFs.

The motivation underpinning the whole analysis presented herein is twofold. Firstly, the approach developed by Adrian and co-workers is not free from shortcomings when applied to OCFs, as it does not explain the mismatch in VLSM vs. LSM scaling, as recently observed by Cameron *et al.* (2017) and Peruzzi *et al.* (2020); hence, new and different approaches to the problem might shed new light on the issue. Secondly, the approach followed by CH is particularly well-suited to study turbulence in OCFs, as this class of flows is not affected by a fundamental problem that makes the same method more convoluted when applied to other wall flows, as explained in the following.

In their earlier studies, CH investigated the hydrodynamic stability of mean velocity profiles pertaining to turbulent wall flows. The aim was to identify the length-scales of perturbations that extract energy directly from the mean flow so that these could be related to turbulent coherent structures, including LSMs and VLSMs (Cossu *et al.* 2009; Pujals *et al.* 2009; Hwang & Cossu 2010; Park *et al.* 2011). This proved to be challenging because any so-called canonical wall-flow is characterized by an asymptotically stable mean velocity profile. Therefore, Hwang & Cossu (2010) analyzed the non-normal transient response of the Orr-Sommerfeld-Squire operator, under the action of a stochastic or periodic body force, and identified the so-called optimal perturbations, namely the perturbations that induce the largest transient response of the perturbation energy (e.g. Schmid & Henningson 2001). The analysis led to the identification of an outer-scaling perturbation displaying longitudinal vorticity, which in subsequent studies was identified as the seed of the outer layer cycle.

Following the approach taken by CH in their earlier studies, the present paper also intends to adopt stability analysis techniques to identify large scale structures in turbulent OCFs. However, with respect to other wall flows, we will demonstrate that the mean velocity profile of OCFs is actually linearly unstable. As will be discussed in depth throughout the paper, this is made possible by the presence of the free surface and by including steady long streamwise cellular structures directly in the mean (i.e., time-averaged) flow. Such structures are commonly referred to as secondary currents and have been reported in the OCF literature since decades and hence their intensity and topology is fairly-well documented (see the recent review by Nikora & Roy 2012). Therefore, in OCFs the cellular structures considered by CH as the key trigger of the outer layer cycle, do not need to be looked for by means of complex transient growth analysis as per other wall flows. They appear directly in the time averaged flow and their effect can be easily included in the steady state equations supporting the base state of the linear stability analysis. This idea sets the compass of the present paper whose general aim is therefore to identify linearly unstable modes of OCFs under the effect of secondary currents displaying a wide range of intensity and topology.

The remaining part of the paper is organized as follows. Sect. 2 provides the structure of the organised secondary flow and the mathematical model of shallow waters. In Sect. 3, the linear stability analysis of the systems is developed through a spectral Galerkin technique. Sect. 4 provides some general results of the analysis. Finally, in Sect. 5 the relationships with the CH-approach is discussed and some conclusions about the physics underlying the observed instability are drawn.

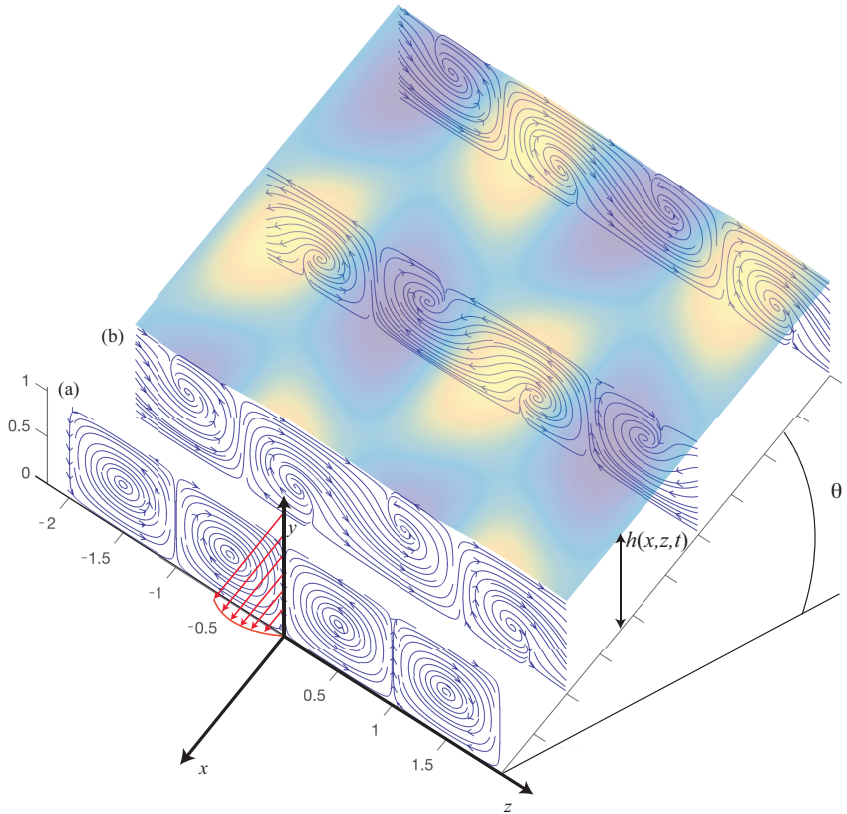


FIGURE 1. Three dimensional view of the flow field. (a) The undisturbed secondary cells. (b) Symmetry breaking of the secondary cells from the perturbative solution under the most unstable conditions ($\omega=0.006$; $\epsilon=0.005$; $L_x=4$; $L_z=2$ ($\beta=\pi$); $F=0.7$; $d=0.01$, see Sect. 3 for details). Color shading refers to the perturbation of the flow field with lows (lighter) and peaks (darker). Red arrows refer to the primary longitudinal flow $\mathcal{F}(y)$.

2. Mathematical model

We will exploit the shallowness of open channel flows in order to tackle the problem at hand with the aid of depth-averaged equations. To this aim, Reynolds-Averaged Navier Stokes equations (RANS) will be integrated along the bed-normal coordinate, by paying attention to preserve dispersive terms arising from the momentum transport coupling between the longitudinal and transverse velocity profile. In the depth-averaged procedure, such dispersive terms will appear in the form of integral factors. This trick is particularly suitable when applied to a flow field that, under undisturbed conditions, is composed by a primary longitudinal flow and a secondary recirculating current (see Fig. 1). The ultimate goal of the present approach is to perform a stability analysis of the secondary currents in order to discuss their role in triggering large-scale turbulence structures. This is usually referred to as a *secondary* stability analysis in Hydrodynamic Stability Theory (e.g. Drazin & Reid 2004; Bertagni *et al.* 2018).

2.1. Framework

Open channel flows can be described by RANS equations flanked by suitable boundary conditions, such as the kinematic and dynamic conditions at the free surface, and the no-slip and impermeability at the bed. We will adopt the bulk longitudinal velocity \hat{U}_0 , the channel depth \hat{h}_0 , the corresponding hydrodynamic timescale \hat{h}_0/\hat{U}_0 , and $\rho\hat{U}_0^2$ to non-dimensionalize velocities, lengths, times and pressure, respectively. Body forces are non-dimensionalized by the module of the gravity acceleration. Henceforth, the hat symbol identifies dimensional quantities.

As reported in the sketch of Figure 1, we consider the (dimensionless) reference frame $x_i=(x, y, z)$, having axes parallel to the streamwise, bed-normal and spanwise directions respectively. The corresponding Reynolds-averaged velocity term is $\mathbf{u}:= (u, v, w)$. Assuming high Reynolds numbers and hence negligible viscous stresses, the non-dimensional RANS equations read as

$$\frac{\partial \mathbf{u}}{\partial t} + \mathbf{u} \cdot \nabla \mathbf{u} + \nabla p + \nabla \cdot \boldsymbol{\tau} - \frac{\mathbf{k}}{F^2} = 0, \quad (2.1)$$

$$\nabla \cdot \mathbf{u} = 0, \quad (2.2)$$

where $F=\hat{U}_0/(g\hat{h}_0)^{1/2}$ is the Froude number, $\boldsymbol{\tau}$ is the dimensionless Reynolds stress tensor, $\mathbf{k}=(\sin \theta, -\cos \theta, 0)$ is the projection of the gravity unit-vector along the chosen coordinate system, with θ being the slope of the bed, with respect to a horizontal plane (see Figure 1).

2.2. Secondary currents of Prandtl's second kind in open channel flow

Secondary currents are cellular structures with longitudinal vorticity (see Figure 1a) that appear in the time-averaged flow. In the present paper, we consider the case of a straight open channel in uniform flow conditions, whereby secondary flows are of Prandtl's second kind as they are the result of a combined effect between the three-dimensionality of the flow imposed by lateral boundaries and the anisotropy of turbulence (Nezu & Nakagawa 1993). Secondary currents are clearly triggered in proximity of lateral boundaries where they occur in the form of 'corner vortices' and are characterized by intense lateral and vertical mean velocities. Their cellular structure then replicates along the lateral direction as a result of mass and momentum conservation, but their intensity fades out while moving towards the center of the channel so much so they become difficult to detect experimentally (Zampiron *et al.* 2020). Nevertheless, Adrian & Marusic (2012) pointed out that even for the case of very wide channels (i.e., channels whose width is much greater than their depth) secondary currents should be present, however weak, even in the mid cross-section.

From a hydrodynamic instability point of view, a classical result indicates that, for a sufficiently shallow rectangular channel, the footprint of secondary currents on the spanwise profile of the streamwise (time-averaged) velocity can be interpreted as a turbulence induced instability. The structure of such an instability in the (y, z) cross section was obtained by Ikeda (1981) and Nezu & Nakagawa (1993) after a term-by-term order of magnitude analysis of the time averaged vorticity budget equation. By imposing a balance between the production of vorticity due to turbulence anisotropy and the suppression of vorticity due to Reynolds shear stress, assuming that the difference in the Reynolds normal stresses is linearly y -distributed, and the bed shear stress is laterally periodically perturbed, Ikeda (1981) came to a solution for the velocity field imposed by secondary currents which, by employing the dimensionless parameters introduced in the

present work, reads as

$$v_0 = -\omega\beta\mathcal{G}(y)\cos(\beta z), \quad w_0 = \omega\frac{d\mathcal{G}(y)}{dy}\sin(\beta z). \quad (2.3)$$

An approximated derivation of (2.3) from equations (2.1), and a general solution for the distribution of the vertical velocity \mathcal{G} is detailed in appendix A. The parameter ω is physically dependent on the Reynolds number and the channel aspect ratio (i.e. the ratio between channel width and depth), that accounts for circulation of the cell. The transverse wavenumber $\beta=2\pi/L_z$ accounts for the lateral spacing of secondary currents. According to Townsend (1976), in the absence of longitudinal bed-forms such as ridges, the dominant cell refers to the case $\beta=\pi$, whereby the cells width and the depth are identical ($L_z/2 = 1$). A cross-stream view of the secondary current structure is shown in Figure 1a.

In the results section, it will be shown that ω is of paramount importance since it accounts for the intensity of secondary cells. In fact, by depth-averaging eq. (2.3) and computing the circulation along a curve \mathcal{L} lying on the plane y - z and embracing a whole cell, we readily obtain that

$$\omega = \frac{1}{2\pi} \left| \oint_{\mathcal{L}} (v_0, w_0) \cdot d\mathbf{x} \right| = \frac{\Omega_x}{2\pi}, \quad \text{and} \quad \omega = \left. \frac{\pi \langle v_0 \rangle}{4 - \pi^2} \right|_{z=0, \beta=\pi}, \quad (2.4)$$

where brackets indicate the depth-averaging operator. Thus ω is proportional to the circulation of the velocity field around a curve embracing a whole cell. From the Stokes theorem, this can be interpreted as the value of the streamwise vorticity averaged over the surface covered by a cell (Ω_x) and hence a proxy for the intensity of secondary currents. It is noteworthy that the above result is independent of the shape of the primary velocity distribution $\mathcal{F}(y)$. Equation (2.4) also shows that this value can be easily obtained by depth averaging the (non dimensional) vertical velocity component v_0 from experimental data.

2.3. Depth-averaged equations

In order to derive the equations describing the dynamics of the problem at hand, we adopt the well-known shallow-water approximation (Tan 1992), whereby \hat{h}_0 is much smaller than the dominant horizontal length-scales. Moreover, we assume that the longitudinal velocity components u can be described by the factorization $u=\mathcal{F}(y)U(x, z, t)$, whereas the lateral velocity component is decomposed into a component related to the secondary current, that is with zero depth-averaging, plus a vertically uniform spanwise component, namely $w=w_0(y, z) + W(x, z, t)$. Therefore U and W are the depth-averaged longitudinal and lateral velocities, respectively. Under these hypotheses and upon depth-averaging, Eq. (2.1) reduces to:

$$\frac{\partial \mathbf{U}}{\partial t} + \mathbf{U} \cdot \nabla_{\perp} \mathbf{U} + \frac{\nabla_{\perp} \zeta}{F^2} - \frac{\nabla_{\perp} \cdot (h \mathbf{T})}{h} - \frac{\boldsymbol{\tau}_b}{h} = 0, \quad (2.5)$$

$$\frac{\partial h}{\partial t} + \nabla_{\perp} \cdot (h \mathbf{U}) = 0, \quad (2.6)$$

where $\mathbf{U}(x, z, t)=\{U, W\}$ is the depth-averaged Reynolds-averaged flow field, $\nabla_{\perp}=\{\partial_x, \partial_z\}$, $\zeta=h-x \sin \theta$ is the free surface elevation, $h(x, z, t)$ is the water-depth, $\boldsymbol{\tau}_b$ is the bottom shear stress and \mathbf{T} is a (2×2) tensor resulting from the sum of the depth-averaged Reynolds stress tensor and the dispersive tensor arising from depth averaging. $\boldsymbol{\tau}_b$ and \mathbf{T}

can be modelled by means of the Chezy's and Boussinesq's formulations as

$$\boldsymbol{\tau}_b = -c_f \mathbf{U} |\mathbf{U}|, \quad (2.7)$$

$$\mathbf{T} = \langle \nu_t (\nabla_{\perp} \mathbf{u}_{\perp} + \nabla_{\perp} \mathbf{u}_{\perp}^T) \rangle - \langle (\mathbf{u}_{\perp} - \mathbf{U}) \otimes (\mathbf{u}_{\perp} - \mathbf{U}) \rangle, \quad (2.8)$$

where $c_f = \sin \theta / F^2$ is the friction factor, which depends on the relative bed roughness $d \cdot h^{-1}$ and the Reynolds number Re , $\mathbf{u}_{\perp} = \{u, w\}$, $\nu_t = \sqrt{c_f} h U \mathcal{N}(y)$ is the eddy viscosity, brackets refer to depth averaging, while \otimes refers to the dyadic product. The shape of function $\mathcal{N}(y)$ that defines the eddy viscosity ν_t will be derived in Section 4. The first term in the r.h.s. of (2.8) accounts for the depth averaging of Reynolds' stresses, while the second one produces the so-called dispersive terms that arise from departure of plug flow conditions.

Two remarks are in order. Firstly, the vector equation (2.5) states the momentum conservation along the longitudinal and transverse directions and it was derived assuming that the vertical momentum conservation reduces to the hydro-static balance $p \sim F^{-2}(h-y)$. This condition is the hallmark of the shallow water equations and it can be shown from a dimensional analysis of the momentum conservation along the vertical direction, that it is constrained to the condition that the channel aspect ratio is much larger than the Froude number. Equation (2.6) states mass continuity after the use of the kinematic condition at the free surface (namely $\partial_t h = w - u_{\perp} \cdot \nabla_{\perp} h$). Second, depth-averaging of the longitudinal velocity provides $\langle \mathcal{F} \rangle = 1$ by construction while $\langle w_0 \rangle \sim \langle d\mathcal{G}/dy \rangle \sim 0$, for $\beta \sim \pi$. From the above remarks, we obtain that Eq. (2.8) reads as

$$\mathbf{T} = \sqrt{c_f} U \begin{pmatrix} \frac{1-\mathcal{I}_4}{\sqrt{c_f}} U + 2h\mathcal{I}_0 \frac{\partial U}{\partial x} & h\mathcal{I}_0 \frac{\partial U}{\partial y} + h\mathcal{I}_1 \frac{\partial W}{\partial x} - \frac{\mathcal{I}_2 \omega \sin(\beta z)}{\sqrt{c_f}} \\ h\mathcal{I}_0 \frac{\partial U}{\partial y} + h\mathcal{I}_1 \frac{\partial W}{\partial x} - \frac{\mathcal{I}_2 \omega \sin(\beta z)}{\sqrt{c_f}} & 2h\mathcal{I}_1 \frac{\partial W}{\partial z} + 2h\mathcal{I}_3 \beta \omega \cos(\beta z) - \frac{\mathcal{I}_5 \omega^2}{U \sqrt{c_f}} [\sin(\beta z)]^2 \end{pmatrix}, \quad (2.9)$$

with

$$\mathcal{I}_0 = \langle \mathcal{F} \mathcal{N} \rangle, \quad \mathcal{I}_1 = \langle \mathcal{N} \rangle, \quad \mathcal{I}_2 = \langle \mathcal{F} \mathcal{G}' \rangle, \quad \mathcal{I}_3 = \langle \mathcal{N} \mathcal{G}' \rangle \sim 0, \quad \mathcal{I}_4 = \langle \mathcal{F}^2 \rangle, \quad \mathcal{I}_5 = \langle \mathcal{G}'^2 \rangle, \quad (2.10)$$

whose exact formulation was obtained upon making a specific choice for \mathcal{F} (see section 4) and is reported in Appendix B.

At the base state ($\partial_t = \partial_x = 0$), after combining (2.3) with (2.5)-(2.9), and recalling that $\omega \ll 1$, it appears that the effect of the secondary currents on the streamwise and spanwise momentum conservation is a z -dependent modulation to the longitudinal velocity and depth, respectively $u_0 = \mathcal{F}(y)U_0(z)$, and $h_0(z)$ with

$$U_0 = 1 - \omega \Phi_1 \cos(\beta z) - \omega^2 \left[\frac{1}{4} \Phi_1^2 - \Phi_2 \cos(2\beta z) \right] + \mathcal{O}(\omega^4), \quad (2.11)$$

$$h_0 = 1 + \frac{1}{2} \omega^2 F^2 \mathcal{I}_5 \cos(2\beta z) + \mathcal{O}(\omega^4), \quad (2.12)$$

where:

$$\Phi_1 = \frac{\beta \mathcal{I}_2}{\sqrt{c_f} (2\sqrt{c_f} + \beta^2 \mathcal{I}_0)}, \quad \Phi_2 = \frac{F^2 \mathcal{I}_5 (c_f - c_{f,h}) (2\sqrt{c_f} + \beta^2 \mathcal{I}_0)^2 + 3\beta^2 \mathcal{I}_2^2}{4\sqrt{c_f} (2\sqrt{c_f} - \beta^2 \mathcal{I}_0)^2 (\sqrt{c_f} + 2\beta^2 \mathcal{I}_0)}, \quad (2.13)$$

with $c_{f,h} = \frac{\partial c_f}{\partial h} |_{h=1}$. Equation (2.11) is crucial for the following analysis since it will be shown that such a transverse modulation, combined with the free surface response, induces an instability of the inflectional type to the secondary currents. It is straightforward to show that the terms of order $\mathcal{O}(\omega^3)$ are zero in the above expansions. It is also worth noticing that equation (2.11) is reminiscent of the spanwise modulation derived by Waleffe

(1995), for the case of streamwise rolls superimposed on a laminar Couette flow. In the following analysis we will neglect the terms of order ω^2 or higher, since they complicate the algebraic treatment without any numerically relevant effect (see Appendix E).

3. Stability analysis

3.1. Perturbative solution

In order to account for large-scale longitudinal meandering of the secondary cell axis, let us consider a time-dependent normal-mode perturbation, by adopting the following putative solution to (2.5)-(2.6)

$$\{U, W, h\} = \{U_0, 0, h_0\} + \epsilon\{U_1(z), W_1(z), h_1(z)\}e^{i\alpha x + \lambda t} + c.c., \quad (3.1)$$

where the base state U_0 and h_0 are provided by (2.11) and (2.12) truncated at order ω , ϵ is a small perturbative parameter, α is the longitudinal wavenumber of the perturbation, λ is its growth rate and *c.c.* refers to complex conjugation.

It is important to remark that under non-uniform and unsteady conditions the friction factor depends on the local value of the depth, through the ratio $d \cdot h^{-1}(x, z, t)$. This aspect is accounted for through a Taylor expansion as follows

$$c_f(h) \sim c_f|_{h=1} + \left. \frac{\partial c_f}{\partial h} \right|_{h=1} (h - 1) = c_{f0} + \epsilon \left. \frac{\partial c_f}{\partial h} \right|_{h=1} h_1 e^{i\alpha x + \lambda t} + c.c., \quad (3.2)$$

where $c_{f0} = c_f|_{h=1}$ is the friction factor computed for the unperturbed flow. After substituting the above ansatz in (2.5)-(2.6) and taking into account (2.7)-(2.13), at the order ϵ we obtain the eigenvalue problem

$$u_* (\mathbf{A} + \omega \mathbf{B}) \mathbf{q} = \lambda \mathbf{q}, \quad (3.3)$$

where $\mathbf{q} = \{U_1, W_1, h_1\}^T$, while $u_* := \sqrt{c_{f0}}$ is the dimensionless friction velocity, and

$$\mathbf{A} = \begin{pmatrix} \mathcal{I}_0 \mathcal{D}^2 - \sigma_0 & i\mathcal{I}_1 \alpha \mathcal{D} & \frac{\sigma_1}{u_*} \\ i\mathcal{I}_0 \alpha \mathcal{D} & 2\mathcal{I}_1 \mathcal{D}^2 - \sigma_4 & -\frac{\mathcal{D}}{u_* F^2} \\ -\frac{i\alpha}{u_*} & -\frac{\mathcal{D}}{u_*} & -\frac{i\alpha}{u_*} \end{pmatrix}, \quad (3.4)$$

$$\mathbf{B} = \begin{pmatrix} \sigma_2 \mathcal{C} + \sigma_9 \mathcal{S} \mathcal{D} - \frac{i\sigma_6}{\alpha} \mathcal{C} \mathcal{D}^2 & -\frac{i\alpha\beta\sigma_8}{2} \mathcal{S} - \frac{\sigma_7\beta}{u_*} \mathcal{S} + \frac{i\alpha\sigma_8}{2} \mathcal{C} \mathcal{D} & \sigma_3 \mathcal{C} + \sigma_9 \mathcal{S} \mathcal{D} \\ \sigma_5 \mathcal{S} + \sigma_6 \mathcal{C} \mathcal{D} & \sigma_7 \sigma_4 \mathcal{C} + \sigma_8 (\mathcal{C} \mathcal{D} - \beta \mathcal{S}) \mathcal{D} & \frac{i\alpha\sigma_9 \mathcal{S}}{u_*} \\ 0 & 0 & \frac{i\alpha\sigma_7 \mathcal{C}}{u_*} \end{pmatrix}. \quad (3.5)$$

In these matrices $\mathcal{D}^n = d^n/dz^n$, $\mathcal{C} = \mathcal{C}(z) = \cos(\beta z)$, $\mathcal{S} = \mathcal{S}(z) = \sin(\beta z)$, while the coefficients σ_i are reported in Appendix C. The presence of the functions \mathcal{C} and \mathcal{S} in \mathbf{B} precludes an analytical solution of (3.3), unless $\omega = 0$.

3.2. Spectral solution of the eigenvalue problem

We firstly consider the mapping $z \rightarrow \xi = \beta z$, so that the operators \mathbf{A} and \mathbf{B} become periodic in the interval $\xi = [0, 2\pi]$. The *differential* eigenvalue problem (3.3) may be solved by a Fourier Galerkin spectral method (see e.g. Canuto *et al.* 2006). Accordingly, a modal representation of the approximate solution with trigonometric polynomials is adopted

$$\mathbf{q} = \sum_{k=-N/2}^{k=N/2} \hat{\mathbf{q}}_k e^{ik\xi}, \quad (3.6)$$

where the cutoff parameter N is an even arbitrarily large integer.

A weak formulation of the problem is obtained by selecting a set of test functions $\psi_{l,n}$ that determine the weights of the residual

$$\int_0^{2\pi} [u_*(\mathbf{A} + \omega\mathbf{B}) - \lambda\mathbf{I}]\mathbf{q}\psi_{l,n}d\xi = 0, \quad (n = -N/2, \dots, N/2; \quad l = 1, \dots, 6). \quad (3.7)$$

A natural choice of the test functions is $\psi_{l,n} = (2\pi)^{-1} \mathbf{v}_l e^{-in\xi}$, where \mathbf{v}_l is any vector of the canonical basis in \mathbb{C}^3 (i.e., one component is equal to 1 or i , all the others 0).

In order to reduce (3.7) to an algebraic eigenvalue problem, let us first observe that by expressing $\cos \xi$ and $\sin \xi$ in terms of exponentials $e^{\pm i\xi}$, one can decompose the matrix \mathbf{B} in (3.7) as

$$\mathbf{B} = e^{-i\xi}\mathbf{B}_{-1} + e^{i\xi}\mathbf{B}_1 = \sum_{j=\pm 1} e^{ij\xi}\mathbf{B}_j, \quad (3.8)$$

where \mathbf{B}_j are the matrices with constant coefficients with respect to ξ , similarly to the matrix \mathbf{A} in (3.4). Hence,

$$\begin{aligned} [u_*(\mathbf{A} + \omega\mathbf{B}) - \lambda\mathbf{I}]\mathbf{q} &= \sum_{k=-N/2}^{N/2} \left[u_*(\mathbf{A} + \omega \sum_{j=\pm 1} e^{ij\xi}\mathbf{B}_j) - \lambda\mathbf{I} \right] e^{ik\xi} \hat{\mathbf{q}}_k \\ &= \sum_{k=-N/2}^{N/2} \left[u_*(\hat{\mathbf{A}}_k + \omega \sum_{j=\pm 1} e^{ij\xi}\hat{\mathbf{B}}_{j,k}) - \lambda\mathbf{I} \right] e^{ik\xi} \hat{\mathbf{q}}_k \\ &= \sum_{k=-N/2}^{N/2} [u_*(\hat{\mathbf{A}}_k \hat{\mathbf{q}}_k e^{ik\xi} + \omega \sum_{j=\pm 1} \hat{\mathbf{B}}_{j,k} \hat{\mathbf{q}}_k e^{i(k+j)\xi}) - \lambda \hat{\mathbf{q}}_k e^{ik\xi}], \end{aligned} \quad (3.9)$$

where the matrices $\hat{\mathbf{A}}_k$, $\hat{\mathbf{B}}_{j,k}$ are obtained from \mathbf{A} , \mathbf{B}_j by replacing the derivative operator $\mathcal{D} = d/d\xi$ by ik (Fourier differentiation). The entries of these matrices are reported in Appendix D.

After substituting (3.9) in (3.7), one easily obtains the algebraic eigenvalue problem of order $3(N+1)$

$$u_*(\hat{\mathbf{A}}_n \hat{\mathbf{q}}_n + \omega \sum_{j=\pm 1} \hat{\mathbf{B}}_{j,n-j} \hat{\mathbf{q}}_{n-j}) = \lambda \hat{\mathbf{q}}_n, \quad (n = -N/2, \dots, N/2). \quad (3.10)$$

Note that the matrix of order $3(N+1)$ corresponding to the left-hand side is block-tridiagonal, with diagonal blocks given by $u_*\hat{\mathbf{A}}_n$ and off-diagonal blocks given by $u_*\omega\hat{\mathbf{B}}_{1,n-1}$ (left), and $u_*\omega\hat{\mathbf{B}}_{-1,n+1}$ (right).

A ready-to-use set of Matlab script for the solution of (3.10) can be found in the Online Supplementary Material.

4. Results

We consider the simplest and most common choice for the velocity distribution, namely the well-known log-law for the mean velocity distribution

$$\mathcal{F} = \frac{\sqrt{c_f}}{\kappa} \log \frac{y}{y_0}, \quad (4.1)$$

where κ is the von Karman's constant and y_0 is the roughness length. By inserting (4.1) in the stream-wise component of (2.1), and accounting for steady uniform flow conditions,

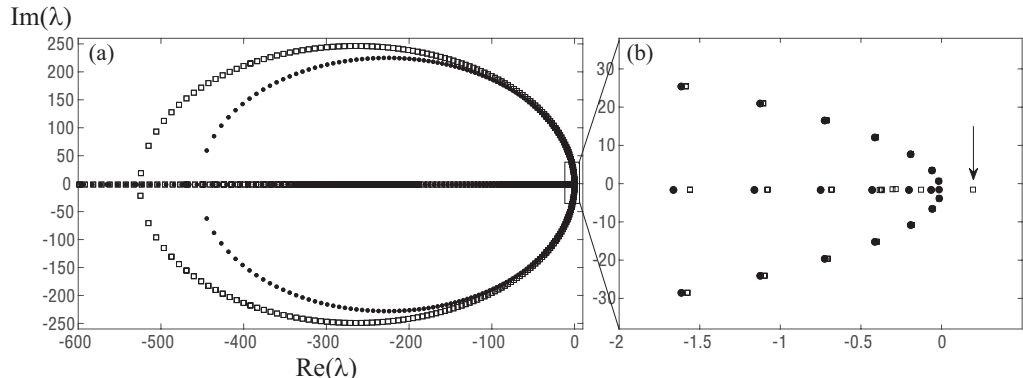


FIGURE 2. (a) Eigenvalue spectra. (b) Zoom in the neighbourhood of the imaginary axis. Close symbols: $\omega=0$; Open symbols: $\omega=0.02$. [$\beta=\pi$; $d = 0.01$; $F=0.7$; $\alpha=\pi/2$; $N=350$]. The arrow indicates the (only) unstable mode.

we obtain

$$y \frac{d\mathcal{N}}{dy} + \kappa y^2 - \mathcal{N} = 0, \quad (4.2)$$

and by imposing zero turbulence on the free surface, $\mathcal{N}(1)=0$, the classical parabolic solution for the eddy viscosity can be recovered, namely, $\mathcal{N}=\kappa y(1-y)$. In addition, $\langle \mathcal{F} \rangle = 1$ by construction, so from (4.1) the friction factor c_f can be computed as

$$\sqrt{c_f} = \frac{\kappa}{\frac{y_0}{h} - 1 - \log \frac{y_0}{h}}. \quad (4.3)$$

In hydraulically-rough bed conditions (very relevant in fluvial environments), the roughness length is usually set proportional to the mean (dimensionless) diameter of the equivalent sediment grain d (or other features of the grain distribution). By setting the equivalence between (4.3) and Strickler's formula for hydraulically rough wall, $\sqrt{c_f} = \sqrt{g} d^{1/6} / 21$, we obtain $y_0 \sim d/15$. Therefore, in this case the friction factor is independent of the Reynolds number.

In summary, the parameter space of the present problem is reduced to: α , β , F , d and ω . The case of hydraulically smooth wall will not be analyzed since it is not relevant to fluvial applications and it has been poorly investigated experimentally. Yet, we have verified that it performs, qualitatively, as the rough wall case.

It is straightforward to show that the case without secondary currents ($\omega=0$) is invariably stable. This case is in fact described by the eigenvalues of the operator \mathbf{A} , which admits eigenfunctions proportional to $\exp(ik\beta z)$ where k is integer. The problem is therefore reduced to the solution of k cubic equations whose roots have all negative real parts, for any k (see black circles in Fig. 2). This result confirms the robustness of the canonical shallow water equations to harmonic perturbations and suggests that there exists a threshold value ω_c of ω that is necessary to trigger the instability of secondary currents (see white squares in Fig. 2b). Through a sensitivity analysis (not show here) we observed that ω_c ranges in a thin interval $[1.4 - 3.2] \cdot 10^{-3}$.

In the case $\omega > 0$, the problem needs to be solved by using the spectral method illustrated in Sect. 3.2. A reliability test for the developed algorithm has validated the exponential convergence in the accuracy of the method versus the cut-off N , showing that 20-30 modes are sufficient to reach machine precision. The relative error has been assessed with respect to the value computed with maximum precision ($N=70$ in Figure 3). Figure 3 identifies two modes of instability that are detected by the present approach.

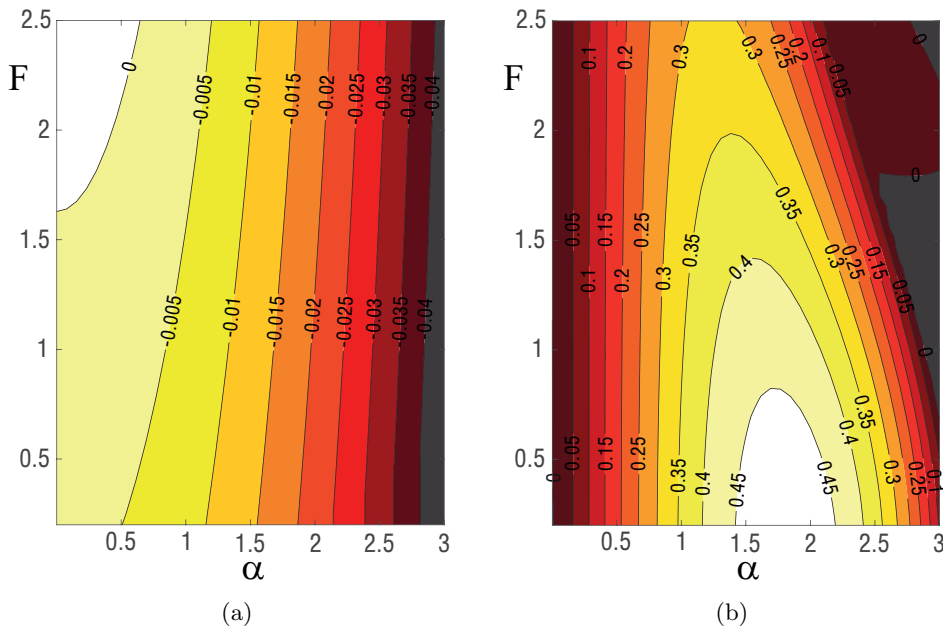


FIGURE 3. Contour-plot of the growth rate $\text{Re}[\lambda_1]$ in the $(\alpha-F)$ plane [$d=0.01$]. (a) Roll-wave mode for $\beta \sim 0$ ($L_z \rightarrow \infty$) and $\omega=0$. (b) Sinuous mode for $\beta=\pi$ ($L_z=2$) and $\omega=0.041$.

The first one is related to the occurrence of roll-waves (panel *a*), which are foreseen at $F > 1.5$, in the limit of infinite lateral spacing of the perturbation ($L_z \rightarrow \infty$). Such cylindrical perturbations of the free surface are typical of very steep beds and are unaffected by secondary currents. The shape of the unstable domain of the roll-waves is reproduced in agreement with other previous theories (Camporeale *et al.* 2012; Caruso *et al.* 2016). Furthermore, the present theory provides an improvement with respect to the classical shallow water theory based on the linearized Saint-Venant equations (Whitham 1974), where roll-wave instability is expected at $F > 2$, for any longitudinal wavelength. In particular, the reduction of the critical Froude number F_c to the value 1.5 is due to Taylor's expansion of the friction factor c_f (eq. 3.2), and provides a result that is consistent with previous linearized approaches. Following a criterion of instability introduced by Dressler (1949), the critical Froude number reads

$$F_c = [\Psi^2 - (2\Psi - 1)\mathcal{I}_4]^{-1/2}, \quad (4.4)$$

where $\Psi = (3 - c_{f,h}/c_{f0})/2$ (see also Arai *et al.* (2013) for a modern treatment). The above equation provides the classical result $F_c=2$ when $c_f=c_{f0}$, $\mathcal{I}_4=1$ and the term $[\partial c_f/\partial h]_{h=1} \equiv c_{f,h}$ is set to zero. On the contrary, when $c_{f,h} \neq 0$, (4.4) gives that F_c decreases from 1.7 to 1.63 for $d=[0.001-0.01]$, that is in agreement with our results.

The second mode of instability (panel *b*) is the main focus of the present paper. It is detected when the spacing between counter-rotating secondary cells is nearly equal to the depth ($L_z=2$) and it is characterized by a symmetry-breaking of the secondary currents induced by the development of waves that are about four depths-long in the stream-wise direction ($L_x=4$, see also Fig. 1b).

The value of the least stable eigenvalue $\lambda \equiv \lambda_1$, as obtained by the spectral method described in Sect. 3.2, is reported versus the longitudinal wavelength $L_x=2\pi\alpha^{-1}$ for various ω values (Fig. 4a). It is evident that the growth rate always displays a maximum

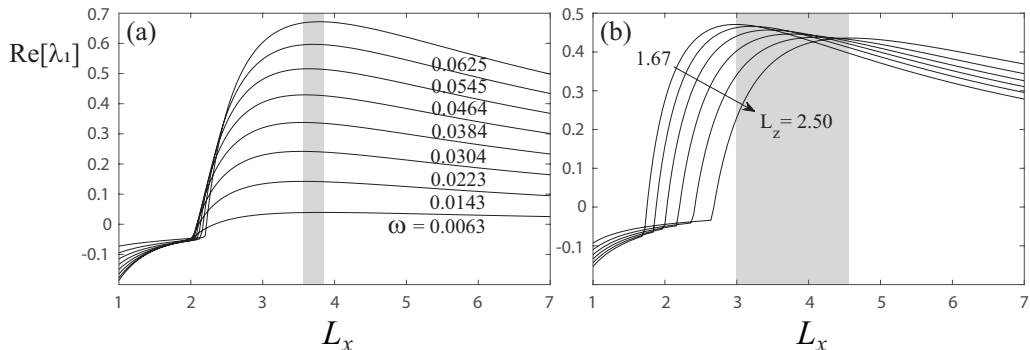


FIGURE 4. (a) Growth rate versus the longitudinal wavelength for: (a) different values of $\omega=[0.006-0.062]$ and $(F, d, L_z)=(0.7, 0.01, 2)$; (b) different values of $L_z=[1.67-2.5]$ and $(F, d, \omega)=(0.7, 0.01, 0.04)$. The shaded areas mark the range of variability of L_x^{max} .

at a particular longitudinal wavelength $L_x=L_x^{max}$ and then decays for longer and shorter wavelengths. This means that the linear stability analysis is able to select a longitudinal wavelength, corresponding to the least stable mode, and the problem is well-posed for larger and smaller length-scales.

The selected wavelength L_x^{max} assumes almost constant values around 3.5-4 times the depth, when the lateral spacing between cells is set to the experimentally observed value $L_z=2\pi/\beta=2$ (i.e., purely circular cells). These values of L_x^{max} are well within the range of those reported for LSMs' wavelengths estimated in the outer layer of rough and smooth bed open channel flows, by Cameron *et al.* (2017) and Peruzzi *et al.* (2020) (note that in both papers the wavelength of LSMs increases with increasing wall distance, from 2 to 6 times the depth). This suggest that LSM-spectral-peaks could be partly caused by an instability of secondary currents that is reminiscent of the sinuous-mode streak instability reported by CH for other wall flows and considered as the trigger of the outer layer cycle (Park *et al.* 2011; Cossu & Hwang 2017). We also notice that this result is quite robust to the choice of the free parameters. In particular, if the lateral spacing L_z is allowed to vary over a broader range ($L_z=[1.5-2.5]$, see Figure 4b), the selected wavelength L_x^{max} remains locked between 3 and 4.5.

We remark that the analysis of the spectrum reveals that the present approach has a limit of validity that is identified by an upper bound on the parameter ω , henceforth referred to as ω_u , above which the problem (3.3) exhibits a set of eigenvalues with positive real part. These eigenvalues are not associated with any physical instability-mode. Yet, it is worth noticing that such shortcomings are not an issue since they have effects when ω is very high, corresponding to nonphysical values of the secondary current magnitude. The threshold value ω_u beyond which our theory is no longer valid can be fairly easily estimated as follows.

Consider the matrices $\hat{\mathbf{A}}_k$ and $\hat{\mathbf{B}}_{\pm 1, k}$ introduced in Sect. 3.2, which appear in the eigenvalue problem (3.10); neglecting the lower-order terms with respect to the wavenumber k , one obtains diagonal matrices with non-zero entries proportional to k^2 , by which an eigenvalue problem similar to (3.10) can be defined. Solving it amounts to computing the eigenvalues of two tridiagonal matrices, whose non-zero entries in the n -th row ($-N/2 \leq n \leq N/2$) are given by

$$\omega b(n-1)^2, \quad an^2, \quad \omega b(n+1)^2 \quad (4.5)$$

for $a = -\mathcal{I}_0\beta^2$, $b = \mathcal{I}_0\Phi_1\beta^2/2$ or $a = -2\mathcal{I}_1\beta^2$, $b = \mathcal{I}_1\Phi_1\beta^2$, where Φ_1 is defined by

(2.13). Then, Gershgorin's Circle Theorem (Golub & Van Loan 1996) guarantees that all such eigenvalues have non-positive real parts provided $\omega \leq \frac{a}{2b} = -\Phi_1^{-1}$; furthermore, clear numerical evidence indicates that positive eigenvalues appear as soon as ω exceeds this threshold. This analysis suggests that the threshold ω_u for the original eigenvalue problem (3.10) should satisfy

$$\omega_u \sim -\Phi_1^{-1}. \quad (4.6)$$

Notice that the above relation depends on the parameters d and β only. Remarkably, a comparison of the right-hand side of (4.6) with the value of ω_u obtained from the numerical solution yields a discrepancy less than 1%, that is completely acceptable for practical purposes. More importantly, when considering the possible range of variation of β and d , it turns out that ω_u is of order 10^{-1} or larger. Upon analysis of the results presented by e.g. Blanckaert *et al.* (2010), such values of ω_u seem significantly higher than those expected in open channel flows over rough beds.

4.1. Inflectional and streak instabilities

The previous results open some questions on the cause-effect connection between the shape of secondary cells and the observed unstable modes. Rayleigh's criterion states that the necessary condition for the instability of a parallel (inviscid) flow is that the basic velocity profile displays an inflection point. Fjørtoft's criterion also adds that the absolute vorticity is maximum at the inflection point (Schmid & Henningson 2001). Due to the presence of inflection points in the transverse profile of the longitudinal flow and $U_0(z)$ satisfying both conditions – see equation (2.11) –, it is worth exploring to what extent the nature of the detected instability has an inflectional nature such as the Kelvin-Helmoltz (KH) kind. In this context, mixing layers satisfy inflectional criteria and trigger KH-instabilities with a temporal frequency $f = a(U_M + U_m)/2\theta$ (Ho *et al.* 1991), where U_M and U_m are the maximum and the minimum of the velocity profile respectively, while θ is the momentum thickness

$$\theta = \frac{1}{4} \int_{z^-}^{z^+} \left[1 - \left(\frac{2U_0 - U_M - U_m}{U_M - U_m} \right)^2 \right] dz, \quad (4.7)$$

with z^- and z^+ setting the boundaries of the profile. The coefficient a is equal to 0.032 in the case of a hyperbolic-tangent velocity profile. Inflectional stability was also studied in the context of jets and vegetated canopies (Raupach & Shaw 2009; Finnigan *et al.* 2009). More recently, by means of long-duration experiments using stereoscopic particle image velocimetry, Zampiron *et al.* (2020) experimentally observed a linear relation between the longitudinal wavelength of the secondary current instability and the vorticity thickness, i.e., $L_x \sim b\delta_\omega$, where

$$\delta_\omega = \frac{U_M - U_m}{\max \left| \frac{dU_0}{dz} \right|}. \quad (4.8)$$

The proportionality constant b was found to be equal to 9 by Zampiron *et al.* (2020) while a value of 15 was obtained by Finnigan *et al.* (2009) for canopy mixing layers and about 4 by Dimotakis & Brown (1976) for canonical mixing layers. It is important to notice, that in the experiments carried out by Zampiron *et al.* (2020) (most relevant for the present paper) secondary currents were amplified by placing longitudinal ridges on the channel bed and hence did not evolve naturally on a flat rigid bottom as in canonical uniform open channel flows.

Because of the periodic nature of $U_0(z)$, the flow field under consideration is subjected to a sequence of inflectional profiles, so it is convenient to set $z^\pm = \pm\pi/\beta$. In this way,

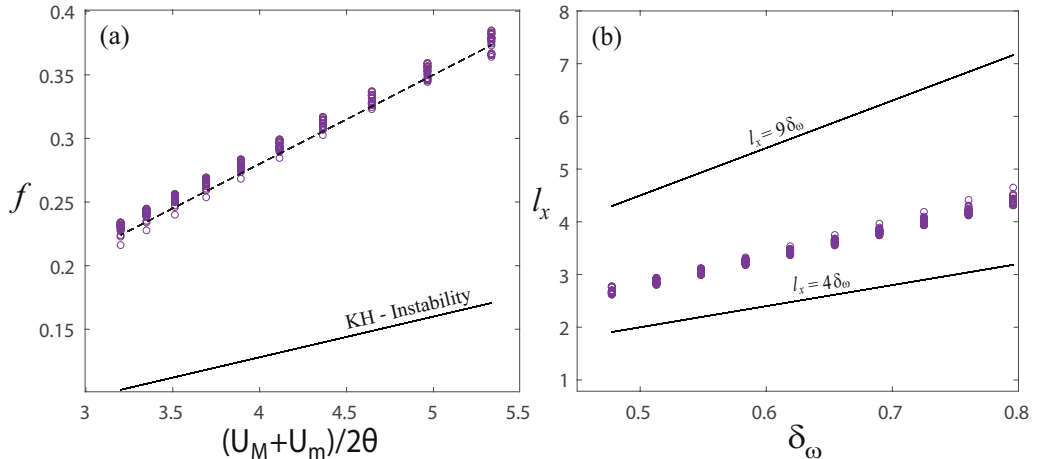


FIGURE 5. Inflectional instability. (a) Relation between the temporal frequency of the least stable wave and the momentum thickness. KH-instability in hyperbolic tangent profile (solid line); our results (dots); $f=0.07(U_M+U_m)/2\theta$ (dashed line). (b) Relation between the selected wavelength and the vorticity thickness. The dashed line refers to best fitting of dots ($F=[0.2-0.8]$; $\omega=[0.005-0.04]$; $L_z=[1.7-2.5]$).

from equations (4.7) and (4.8) we obtain, respectively,

$$\theta = \frac{\pi}{4\beta}, \quad \delta_\omega = \frac{2}{\beta}. \quad (4.9)$$

Figure 5a and b report the instability frequency and the selected wavelengths versus $(U_M + U_m)/2\theta$ and vorticity thickness, respectively, by spanning the whole range of (F, ω, L_z) values investigated herein. We see that the present problem develops a temporal frequency $f \equiv \text{Im}(\lambda_1)$ that is in fact linearly related to the ratio between the mean velocity and the momentum thickness and the best fitting is $f=0.07(U_M+U_m)/2\theta$ (dashed line in Fig. 5a). Similarly, when the same data are reported in the $\delta_\omega - L_x$ plane (Fig. 5b) a linear relation between the selected wavelength and the vorticity thickness is also confirmed, with a proportionality constant around 6, which is between the values reported by the case of mixing layers and the experiments by Zampiron *et al.* (2020).

The linear relations depicted in Figure 5 suggest that the detected sinuous instability might be of inflectional nature. Indeed, if the spanwise transport of the longitudinal momentum due to lateral gradients $W\partial U/\partial z$ is inhibited – i.e. the second term of the entry B_{12} in equation (3.5) is removed – then the mathematical problem becomes unconditionally stable. However, as it will be pointed out in the subsequent discussion, the inflectional point alone is not a sufficient condition to trigger such an instability, because the presence of a free surface dynamically responding to perturbations is another key requirement.

Another fundamental instability that our work needs to be put into context with, is the so-called *streak instability*, which is strictly linked with the well known near-wall cycle and *self-sustained process* cycle (SSP) investigated by Waleffe (1995, 1997) in the case of laminar flows. Following the success of Waleffe’s works, other authors have considered large-scale optimal streaks, and performed secondary stability analyses in turbulent closed channels flows, by focusing on the outer layer (Park *et al.* 2011) or on the log-layer (Alizard 2015). The usage of solution (2.3) as the starting step of a stability analysis and its connection to turbulence anisotropy sets further similarities with the vortex-wave interaction theory (Hall & Smith 1988, 1991; Waleffe 2010; Hall

2018), where long-wavelength coherent structures support the coexistence of rolls, streaks and waves. Resemblances of our results with those findings are encouraging, and might suggest to frame the present instability in the context of streak secondary instability. However, the depth-averaged approach herein adopted hides a close connection with the three-dimensional framework of the mentioned works.

As explained in the subsequent discussion, the key role of the free surface in making the difference with respect to both streak instabilities (as performed by CH and Alizard (2015)) and the KH instability will be commented, suggesting that the right interpretation might be in between.

5. Discussion

In order to put the results obtained herein for open channel flows within the wider context of wall flows, analogies and differences between the present work and those by CH are now identified and discussed.

Firstly, it is important to point out that with respect to the CH approach, the proposed procedure does not require a transient growth analysis. The fact that OCFs develop steady secondary flow structures relieves the mathematical methodology from adopting non-normal analyses to identify optimal perturbations as the seedling of instabilities and permits to keep the whole work within the remit of canonical linear stability analysis. In this context it is instructive to compare the present base state and the outcomes of the non-normal analyses previously developed by CH. In Hwang & Cossu (2010), the optimal transient perturbation of the flow field was generated by a body force artificially added to the linearised governing equations for closed channel flows. This *optimal* body force is distributed within the flow domain in the form of counter-rotating cells with an aspect ratio close to one (see arrays in Figure 6a). In the original scaling adopted for closed channels, where δ is taken as the half-distance between plates, perfect circularity would correspond to $\hat{L}_z \sim 4\delta$, while the exact value reported by the authors was $\hat{L}_z = 3.5\delta$. This suggests that in the CH-approach the external body force somewhat plays a similar role to the secondary currents (v_0, w_0) considered in eq. (2.3) in being the trigger of the instability. The stream-wise velocity u_0 , whose lateral structure is reported in equation (2.11) is akin to the outer longitudinal streaks detected in the transient analysis (contour-lines in Fig. 6b). Note that secondary currents have a different topology with respect to the transient and body-forced-induced velocity pattern reported in closed channels by CH (see Figure 6). In CH lines of constant longitudinal velocity are closed and anti-symmetrical with respect to the horizontal mid plane. In our study the same lines are bounded by the free surface. It is also important to remind that in Hwang & Cossu (2010) the longitudinal streaks, which correspond to optimal perturbations, although being detected at vanishing values of the temporal frequency and longitudinal wavenumber, they are a transient response of the system, while the secondary currents are features of the time-averaged flow.

Both the present stability analysis and the works by CH detect scales of motion comparable, in size, to LSMs, by resolving the response of the systems to the injection of an organised cellular structure (i.e., the optimal perturbation in the former, secondary currents in the latter). In both cases, the response of the system was identified to be sensitive to the intensity of the organised structure. In particular, de Giovanetti *et al.* (2017) defined a measure of the streak amplitude A_s^+ , which is related to the control parameter ω as

$$A_s^+ = \frac{|\Phi_1|}{u_*} \omega \quad (5.1)$$

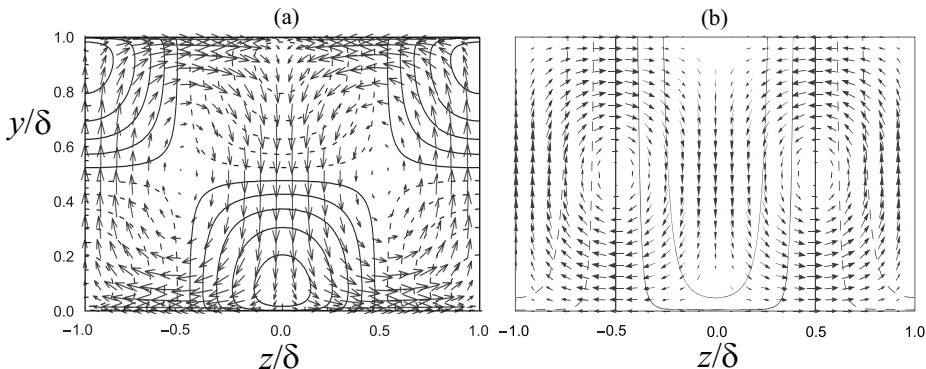


FIGURE 6. (a) Cross-stream view of the optimal forcing (arrows) and the corresponding response in the streamwise velocity (contours) from the transient growth analysis in close channel flows (adapted from Hwang & Cossu 2010). (b) Cross-stream view of the secondary currents (arrows) described by eq. (2.3) and the corresponding response in the stream-wise velocity (contours). In both panels solid contours refer to positive values, negative contours to negative values, while the quantity δ refers to the channel depth.

with Φ_1 defined by (2.13). The same authors realized that the premultiplied spectral intensity of wall-normal velocity in the core of the flow for $L_x = 3.57\delta$ abruptly increases when $A_s^+ > 4$. From (5.1) this threshold corresponds to $\omega = 0.012$ when $d = 0.001$. We detected that the critical values ω_c for the occurrence of the linear instability are of order 10^{-3} , which suggests that OCFs are usually more unstable to LSMs than closed channel flows. Incidentally, we notice that coupling equations (4.6) and (5.1), with $\omega = \omega_u$, it is easy to show that $A_{s,u}^+ = c_{f0}^{-1/2}$. We remind that the latter term depends on the wall roughness only, and it is usually larger than 10. This means that the present theory is valid as long as $A_s^+ \lesssim 10$.

It remains to explain the reason why a linear stability analysis of depth-averaged equations is sufficient to detect instabilities at wavelengths comparable to those of LSMs for OCFs, in place of the sophisticated non linear simulations adopted in closed channels. To this end, it is interesting to observe that, if the stability analysis is replicated under *the rigid lid approximation*, that is by artificially eliminating the dynamic character of the free surface (i.e., by forcing $h_1 = 0$), then the problem turns to be unconditionally stable, as it is evident in Figure 7a. Therefore, the free surface plays a crucial role in triggering the linear instability, an aspect that is precluded to closed channel flows. From a qualitative perspective, it is straightforward to show that the instability mechanism resides in the capability of the free surface to behave as a linear resonator which amplifies the hydrodynamic perturbations. If we in fact consider the depth-averaged linearised continuity equation and neglect for simplicity the $\mathcal{O}(\omega)$ terms, after a further averaging across the spanwise direction over the interval $z = [-0.5, 0.5]\pi\beta^{-1}$, we obtain

$$\frac{\partial \bar{h}}{\partial t} = \frac{\partial \bar{U}}{\partial x} + \beta \bar{W} + \frac{\partial \bar{h}}{\partial x}, \quad (5.2)$$

where the overbar symbol refers to the spanwise averaging. Let us then analyze the response of an initial meander-like perturbation of the axis of the secondary cell, as reported in Figure 7c, while initially considering an unperturbed free-surface. Panel d shows that the streamwise and spanwise velocities associated with this perturbation are phase-lagged. Instead, the first and second terms in the right hand side of eq. (5.2) result in-phase and they both force an alternation of growth and decay of the free surface

along x , as reported in Figure 7d. Such a response in the free surface has two effects: i) the activation of the last term in the right hand side of (5.2), which triggers the characteristic kinematic waves on the free surface, with the phase-celerity of order 1 (in non-dimensional units); ii) a stream-wise gradient pressure $-d\bar{h}/dx$ that, thanks to the momentum equation, reinforces the initial velocity perturbation. The latter effect indicates a potential mechanism for the amplification of the hydrodynamic perturbations driven by momentum and mass conservation principles. In open-channel flows, this mechanism is known to be the driver of different kinds of instabilities (Camporeale & Ridolfi 2012; Camporeale *et al.* 2013; Camporeale 2015) and might justify the linear growth of the sinuous-mode instability observed herein.

To complete the picture, we also remind that the inflectional character of the instability, that has been discussed in Sect. 4.1, has a purely hydrodynamic (i.e., no connection with the free surface) and frictionless nature. Our final interpretation is that the inflectional character of the stream-wise velocity is crucial in triggering the instability at the lateral length-scale of the longitudinal vortices – through the convective term $W\partial U/\partial z$ – but it is not sufficient when turbulent diffusion is considered. In fact, the free surface plays a key role as amplifier of the instability, while the spanwise turbulent momentum transport stabilizes the process. The trade off appears at the LSM longitudinal length-scales when both mechanisms are present. This picture is confirmed by computing again the least stable mode under the rigid lid approximation, plus neglecting the lateral turbulent momentum transport (i.e., null eddy viscosity in eq. (2.8), equivalent to set $\mathcal{I}_0=\mathcal{I}_1=0$). The result, reported in Figure 7b, shows the emergence of a dominant maximum growth rate at very small wavelength (order $L_x \sim 1$) and a group of secondary maxima around $L_x \sim 2$, both being significantly smaller than those found considering diffusive effects. In other words, without the damping effect of the eddy viscosity, a meander-like instability induced by secondary currents is exhibited by the system even in the absence of a dynamic free surface, but at length-scales shorter than those associated with LSMs (compare Fig. 7b with Fig. 4a).

6. Conclusions

We have carried out a linear stability analysis of depth-averaged turbulent open channel flows with secondary currents. The adopted strategy was essentially based on three fundamental pillars: i) the use of the simplified pattern proposed by Ikeda (1981) – equations (2.3) – to model the cellular secondary structure; ii) the factorization of the horizontal velocity components and the depth-averaging of the RANS equation under the shallow-water approximation (this aspect allowed for the identification of the spanwise modulation of the stream-wise velocity due to the secondary currents, see eq. 2.11); iii) a linear stability analysis of the shallow water equations around the secondary-flow base state, leading to an eigenvalue problem that was solved by a Fourier Galerkin spectral method.

The analysis led to the identification of sinuous instabilities having wavelengths that are very similar to those pertaining to LSMs, as reported in recent experimental works (Cameron *et al.* 2017; Zhang *et al.* 2019; Duan *et al.* 2020; Peruzzi *et al.* 2020; Duan *et al.* 2021). Such wavelengths are also fairly independent of the choice of other free parameters such as the lateral spacing of the secondary-currents' cells and the Froude number. The results also indicate that, in order to occur, the sinuous instability requires that the circulation of the secondary currents is greater than a critical value ω_c , which is of the order 10^{-3} . It is important to notice that these values are extremely small and correspond to secondary currents having vertical velocities being 0.1% of U_0 . From an

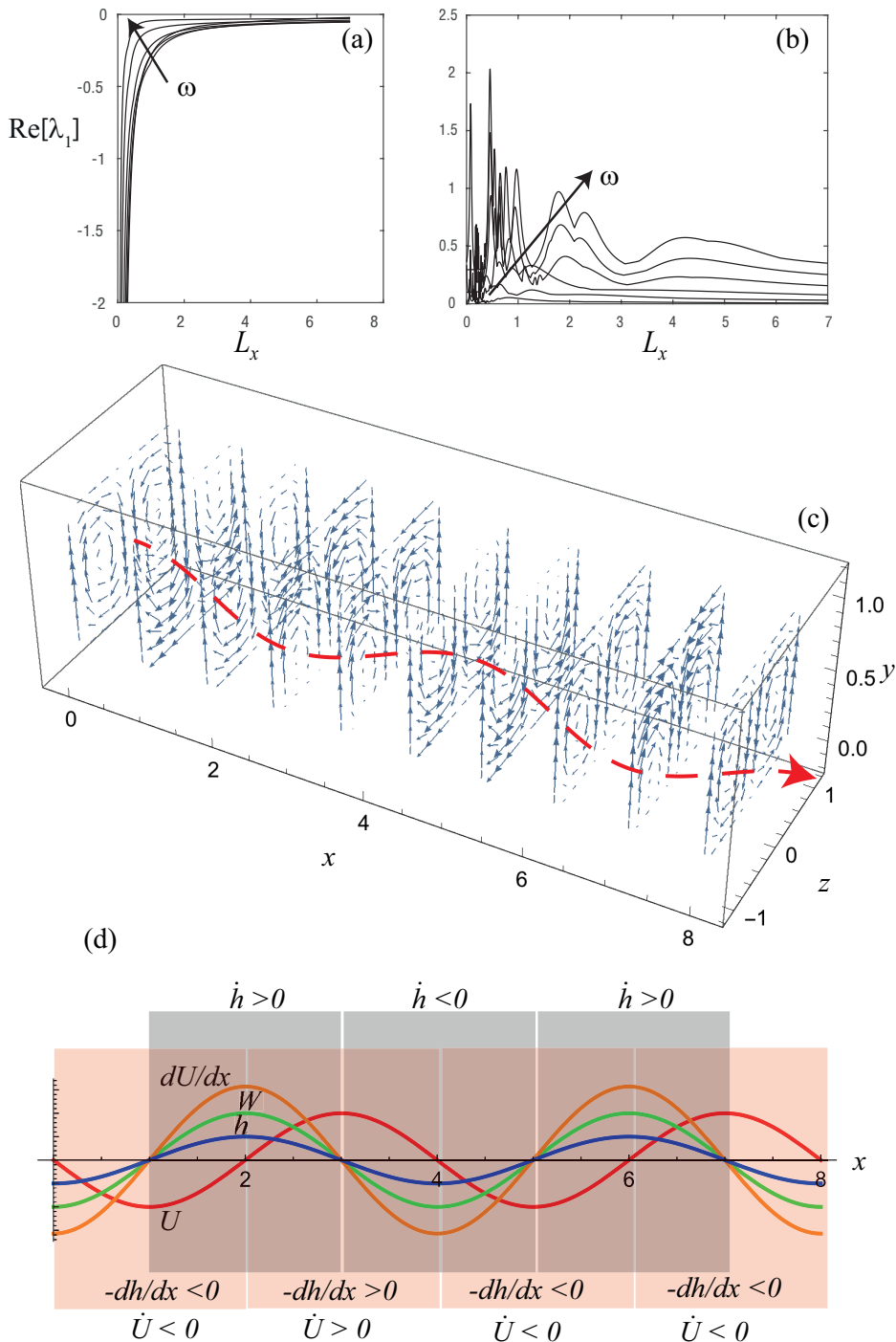


FIGURE 7. Role of the free surface and turbulent dissipation. (a) Growth rate versus the longitudinal wavelength for different values of $\omega=[0.006-0.06]$ and $(d, L_z)=(0.01, 2)$ under the rigid lid approximation ($h_1=0$). (b) As panel (a) but without lateral turbulent diffusion. (c,d) Mechanism of the free-surface amplification for sinuous instability of the secondary currents. (c) Three dimensional view of secondary currents. The red line mark the perturbed axis of the counter-rotating system. (d) Longitudinal profiles of the terms involved in equation (5.2).

experimental point of view, it is extremely difficult to measure, with enough confidence, such small mean velocities in a flume. Hence these results suggest that, even if secondary currents are hardly detectable (as in the mid cross section of the smooth homogeneous bed experiments of Zampiron *et al.* (2020)), they might still exist and have an effect on triggering large eddies akin in size to LSMs. It should hence be pointed out that, while our preliminary results suggest for the existence of a CH-type outer layer cycle triggered by secondary currents, other potential mechanisms driving the formation of LSMs, such as hairpin eddy alignment cannot and should not be ruled out.

As a final remark, our results show that while the linear stability analysis is able to provide a plausible explanation for the occurrence of LSMs in open channel flows, it fails completely in detecting VLSMs. This had to be expected because, even in the works by CH, VLSMs could be detected only when non-linearity effects were taken into account. Indeed, within the context of the outer (but also the buffer-layer) cycle, non linear interactions are a key requirement to damp the divergence of sinuous instabilities and to re-establish the occurrence of longitudinal streaks at very long wavelengths. Therefore, working upon the present paper, future efforts by the authors will focus on identifying suitable analyses able to capture the key non-linear interactions that lead to the formation of VLSMs in open channel flows.

Declaration of Interests.

The authors report no conflict of interest.

Appendix A. Derivation of equation (2.3)

By defining the vorticity as $\boldsymbol{\Omega} = \nabla \times \mathbf{u}$ and using the vector identity $\nabla \times (\boldsymbol{\Omega} \times \mathbf{u}) = \mathbf{u} \cdot \nabla \boldsymbol{\Omega} - \boldsymbol{\Omega} \cdot \nabla \mathbf{u}$, we take the curl of equation (2.1) and assume steady and uniform conditions (i.e., $\partial_t = \partial_x = 0$). In the streamwise direction we get

$$u_y \frac{\partial \Omega_x}{\partial y} + u_z \frac{\partial \Omega_x}{\partial z} - \Omega_y \frac{\partial u_x}{\partial y} - \Omega_z \frac{\partial u_x}{\partial z} = \frac{\partial^2}{\partial y \partial z} (\tau_{yy} - \tau_{zz}) + \left(\frac{\partial^2}{\partial z^2} - \frac{\partial^2}{\partial y^2} \right) \tau_{yz}, \quad (\text{A } 1)$$

where all terms are intended as Reynolds-averaged and τ_{ij} are the components of the Reynolds stress tensor. On the basis of several experimental (Gessner & Jones 1965; Nezu & Nakagawa 1984) and numerical (Demuren & Rodi 1984) evidences, the dominant terms of the above equation are in the r.h.s, namely the streamwise vorticity production due to turbulent anisotropy is balanced by its turbulent suppression. Ikeda (1981) obtained a simple analytical solution by assuming that $\tau_{yz} \sim \langle \nu_t \rangle (\partial_z v_0 + \partial_y w_0)$ (e.g., Ikeda 1981; McLean 1981) and that the turbulent anisotropy term is linearly distributed on the vertical direction and is periodic in the spanwise direction with wavenumber β (e.g. Perkins 1970; Gerard 1978), namely

$$\tau_{zz} - \tau_{yy} = (1 - y) [c_f + \omega \langle \nu_t \rangle \beta^3 \cos(\beta z)]. \quad (\text{A } 2)$$

Notice that the parameter ω , defined in the main text through (2.4), appears now as the rescaled amplitude of the bed shear stress modulation. We also remind that experimental observations report $\beta \sim \pi$. After introducing the stream function $\Psi(y, z)$, such that $v_0 = \partial_z \Psi$ and $w_0 = -\partial_y \Psi$ in force of the continuity equation, the above considerations reduces equation (A 1) to

$$\left(\frac{\partial^2}{\partial z^2} - \frac{\partial^2}{\partial y^2} \right)^2 \Psi = \omega \beta^4 \sin \beta z. \quad (\text{A } 3)$$

The structure of the r.h.s of the above equation suggests the solution $\Psi(y, z) = \omega \mathcal{G}(y) \sin \beta z$, from which we obtain

$$\mathcal{G}^{(iv)} + 2\beta^2 \mathcal{G}'' + \beta^4 \mathcal{G} = \beta^4, \quad (\text{A } 4)$$

where dash refers to y -derivative. A real non-divergent solution of (A 4) satisfying the impermeability condition at the boundaries (i.e., $\mathcal{G}(0) = \mathcal{G}(1) = 0$) is

$$\mathcal{G}(y) = 1 + (y - y \sec \beta - 1) \cos(\beta y). \quad (\text{A } 5)$$

The latter solution reduces to the formulas reported by Ikeda (1981) for channels having finite width, when $\beta = n\pi$ and $\beta = (2n-1)\pi$, with $n \in \mathbb{N}$.

Appendix B. Integral factors

The use of (4.1-4.3) allows one to obtain the following expression for the integral factors:

$$\mathcal{I}_0 = -\frac{\kappa [(4y_0 - 9)y_0^2 + 6 \log y_0 + 5]}{36(y_0 - \log y_0 - 1)}, \quad (\text{B } 1)$$

$$\mathcal{I}_1 = \frac{\kappa}{6}, \quad (\text{B } 2)$$

$$\mathcal{I}_2 = \frac{\beta \text{Ci}[\beta] - \beta [\text{Ci}[\beta y_0] - \log y_0] + 2 \sin^2 \frac{\beta}{2} \sec \beta [\sin \beta - \sin(\beta y_0)]}{\beta (y_0 - \log y_0 - 1)}, \quad (\text{B } 3)$$

$$\mathcal{I}_3 = -\frac{\kappa \tan \beta (\beta^2 + \beta \sin \beta + 4 \cos \beta - 4)}{\beta^3}, \quad (\text{B } 4)$$

$$\mathcal{I}_4 = \frac{2 - 2y_0 + (2 + \log y_0) \log y_0}{(1 - y_0 + \log y_0)^2}, \quad (\text{B } 5)$$

$$\begin{aligned} \mathcal{I}_5 = & \frac{\sec^2 \beta}{96\beta} \{ \beta^3 [16 \cos \beta + 8 \cos 2\beta + 24] \\ & + \beta [-132 \cos \beta + 60 \cos 2\beta - 12 \cos 3\beta + 84] \\ & - 12 \sin(\beta) + 18 \sin(2\beta) - 12 \sin 3\beta + 3 \sin 4\beta - 24 \beta^2 \sin 2\beta \}. \end{aligned} \quad (\text{B } 6)$$

where $\text{Ci}[\dots]$ is the Cosine Integral function.

Appendix C. Coefficients σ_i

$$\sigma_0 = 2u_* + \frac{i\alpha}{u_*} (2\mathcal{I}_4 - 1) + 2\mathcal{I}_0 \alpha^2, \quad \sigma_1 = u_* - \frac{c_{f,h}}{u_*} + \frac{i\alpha}{u_*} \left(1 - \frac{1}{F^2} - \mathcal{I}_4 \right), \quad (\text{C } 1)$$

$$\sigma_2 = \frac{\alpha(2\alpha\mathcal{I}_0 u_* + 2i\mathcal{I}_4 - i)\Phi_1}{u_*}, \quad \sigma_3 = \frac{[2c_{f,h} + \beta^2 \mathcal{I}_0 u_* + 2i\alpha(\mathcal{I}_4 - 1) - 2u_*^2] \Phi_1}{u_*} \quad (\text{C } 2)$$

$$\sigma_4 = u_* + \frac{i\alpha}{u_*} + \mathcal{I}_1 \alpha^2, \quad \sigma_5 = -\frac{2i\alpha u_* \Phi_1}{\beta}, \quad \sigma_6 = -i\mathcal{I}_0 \alpha \Phi_1, \quad \sigma_7 = \frac{\Phi_1}{2}, \quad (\text{C } 3)$$

$$\sigma_8 = -\frac{\mathcal{I}_1 \Phi_1}{2}, \quad \sigma_9 = \frac{\mathcal{I}_2}{u_*} - \frac{4}{\beta^2 \mathcal{I}_0 + 2u_*}, \quad (\text{C } 4)$$

where $c_{f,h} = \frac{\partial c_f}{\partial h} \Big|_{h=1}$, Φ_1 is defined by (2.13) and we remind that u_* is the dimensionless friction velocity, i.e., $u_* = \hat{u}_*/\hat{U}_0 = \sqrt{c_{f0}}$.

Appendix D. Matrices $\hat{\mathbf{A}}_k$ and $\hat{\mathbf{B}}_{j,k}$

$$\hat{\mathbf{A}}_k = \begin{pmatrix} -\mathcal{I}_0 k^2 \beta^2 - \sigma_0 & -\mathcal{I}_1 k \alpha \beta & \frac{\sigma_1}{F^2 u_*} \\ -\mathcal{I}_0 k \alpha \beta & -2\mathcal{I}_1 k^2 \beta^2 - \sigma_4 & -\frac{ik\beta}{F^2 u_*} \\ -\frac{i\alpha}{u_*} & -\frac{ik\beta}{u_*} & -\frac{i\alpha}{u_*} \end{pmatrix} \quad (\text{D } 1)$$

$$\hat{\mathbf{B}}_{-1,k} = \begin{pmatrix} \frac{\sigma_2}{2} - \frac{\beta k \sigma_9}{2} + \frac{i\beta^2 k^2 \sigma_6}{2\alpha} & \frac{\alpha \beta \sigma_8}{4} - \frac{\alpha \beta k \sigma_8}{4} - \frac{i\beta \sigma_7}{2u_*} & \frac{\sigma_3}{2} - \frac{\beta k \sigma_9}{2} \\ \frac{i\sigma_5}{2} + \frac{ik}{2} \beta \sigma_6 & \frac{\sigma_4 \sigma_7}{2} - \frac{\beta^2 k^2 \sigma_8}{2} + \frac{\beta^2 k \sigma_8}{2} & -\frac{\alpha \sigma_9}{2} \\ 0 & 0 & \frac{i\alpha \sigma_7}{2u_*} \end{pmatrix}, \quad (\text{D } 2)$$

$$\hat{\mathbf{B}}_{1,k} = \begin{pmatrix} \frac{\sigma_2}{2} + \frac{\beta k \sigma_9}{2} + \frac{i\beta^2 k^2 \sigma_6}{2\alpha} & -\frac{\alpha \beta \sigma_8}{4} - \frac{\alpha \beta k \sigma_8}{4} + \frac{i\beta \sigma_7}{2u_*} & \frac{\sigma_3}{2} + \frac{\beta k \sigma_9}{2} \\ -\frac{i\sigma_5}{2} + \frac{ik}{2} \beta \sigma_6 & \frac{\sigma_4 \sigma_7}{2} - \frac{\beta^2 k^2 \sigma_8}{2} - \frac{\beta^2 k \sigma_8}{2} & \frac{\alpha \sigma_9}{2} \\ 0 & 0 & \frac{i\alpha \sigma_7}{2u_*} \end{pmatrix}. \quad (\text{D } 3)$$

Appendix E. Effect of terms $\mathcal{O}(\omega^2)$

The theory presented can be improved to order ω^2 . After repeating the same procedure developed in Sect. 3, one obtains that the algebraic eigenvalue problem (3.10) becomes

$$u_* (\hat{\mathbf{A}}_n \hat{\mathbf{q}}_n + \omega \sum_{j=\pm 1} \hat{\mathbf{B}}_{j,n-j} \hat{\mathbf{q}}_{n-j} + \omega^2 \sum_{j=0,\pm 2} \hat{\mathbf{C}}_{j,n-j} \hat{\mathbf{q}}_{n-j}) = \lambda \hat{\mathbf{q}}_n, \quad (n = -N/2, \dots, N/2), \quad (\text{E } 1)$$

where the matrices $\hat{\mathbf{A}}_k$, $\hat{\mathbf{B}}_{j,k}$ are reported in Appendix D, whereas the matrices $\hat{\mathbf{C}}_{j,k}$ are

$$\hat{\mathbf{C}}_{0,k} = \begin{pmatrix} \sigma_{10} - k^2 \beta^2 \sigma_{18} & ik\beta \sigma_{15} & 0 \\ ik\beta \sigma_{24} & \sigma_{21} + \frac{2i\beta^2 k^2 \sigma_{15}}{\alpha} & \frac{i\beta k \sigma_{27}}{2} \\ 0 & 0 & \sigma_{31} \end{pmatrix}, \quad (\text{E } 2)$$

$$\hat{\mathbf{C}}_{-2,k} = \begin{pmatrix} -\frac{\beta^2 k^2 \sigma_{19}}{2} - \frac{\beta k \sigma_{14}}{2} + \frac{\sigma_{11}}{2} & \frac{i\beta k \sigma_{16}}{2} + \frac{i\sigma_{12}}{2} & \frac{\sigma_{13}}{2} - \frac{\beta k \sigma_{17}}{2} \\ \frac{i\beta k \sigma_{25}}{2} + \frac{i\sigma_{20}}{2} & -\frac{\beta^2 k^2 \sigma_{28}}{2} - \frac{\beta k \sigma_{26}}{2} + \frac{\sigma_{22}}{2} & \frac{i\sigma_{23}}{2} - \frac{i\beta k \sigma_{27}}{4} \\ \frac{\sigma_{29}}{2} & \frac{i\beta k \sigma_{33}}{2} + \frac{i\sigma_{30}}{2} & \frac{\sigma_{32}}{2} \end{pmatrix}, \quad (\text{E } 3)$$

$$\hat{\mathbf{C}}_{2,k} = \begin{pmatrix} -\frac{\beta^2 k^2 \sigma_{19}}{2} + \frac{\beta k \sigma_{14}}{2} + \frac{\sigma_{11}}{2} & \frac{i\beta k \sigma_{16}}{2} - \frac{i\sigma_{12}}{2} & \frac{\sigma_{13}}{2} + \frac{\beta k \sigma_{17}}{2} \\ \frac{i\beta k \sigma_{25}}{2} - \frac{i\sigma_{20}}{2} & -\frac{\beta^2 k^2 \sigma_{28}}{2} + \frac{\beta k \sigma_{26}}{2} + \frac{\sigma_{22}}{2} & -\frac{i\sigma_{23}}{2} - \frac{i\beta k \sigma_{27}}{4} \\ \frac{\sigma_{29}}{2} & \frac{i\beta k \sigma_{33}}{2} - \frac{i\sigma_{30}}{2} & \frac{\sigma_{32}}{2} \end{pmatrix}, \quad (\text{E } 4)$$

in which the additional coefficients σ_i are reported in a Supplementary Online Material for the sake of the space.

Figure 8 shows the relative difference between the low-order model ($\mathcal{O}(\omega)$ truncation) and the high-order model ($\mathcal{O}(\omega^2)$ truncation) in the computation of the real part of least stable eigenvalue, for the range of interest of the longitudinal wavelengths L_x . The relative error is generally quite low, so the upgrade of the theory to $\mathcal{O}(\omega^2)$ complicates significantly the algebraic treatment, without a significant gain in the accuracy of the results.

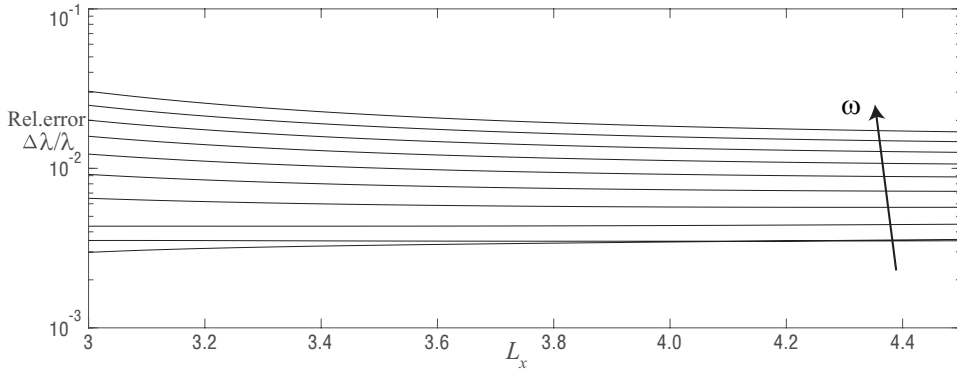


FIGURE 8. Relative difference between the low-order model and the high-order model in the computation of the real part of the least stable eigenvalue for different values of ω and $(F, d, L_z)=(0.7, 0.01, 2)$.

- ADRIAN, R 2007 Hairpin vortex organization in wall turbulence. *Phys. Fluids* **19**.
- ADRIAN, R & MARUSIC, I 2012 Coherent structures in flow over hydraulic engineering surfaces. *J. Hydraul. Res.* **50**.
- ALIZARD, F. 2015 Linear stability of optimal streaks in the log-layer of turbulent channel flows. *Phys. Fluids* **27** (10), 105103.
- ARAI, M., HUEBL, J. & KAITNA, R. 2013 Occurrence conditions of roll waves for three grain-fluid models and comparison with results from experiments and field observation. *Geophys J. Int.* **195** (3), 1464–1480.
- BAGHERIMYAB, F. & LEMMIN, U. 2018 Large-scale coherent flow structures in rough-bed open-channel flow observed in fluctuations of three-dimensional velocity, skin friction and bed pressure. *J. Hydraul. Res.* **56**, 1–19.
- BERTAGNI, M.B., PERONA, P. & CAMPOREALE, C. 2018 Parametric transitions between bare and vegetated states in water-driven patterns. *P. Natl. Acad. Sci. USA* **115** (32), 8125–8130.
- BLANCKAERT, K, DUARTE, A. & SCHLEISS, A.J. 2010 Influence of shallowness, bank inclination and bank roughness on the variability of flow patterns and boundary shear stress due to secondary currents in straight open-channels. *Adv. Water Resour.* **33** (9), 1062–1074.
- CAMERON, S. M., NIKORA, V. I. & STEWART, M. T. 2017 Very-large-scale motions in rough-bed open-channel flow. *J. Fluid Mech.* **814**, 416–429.
- CAMPOREALE, C. 2015 Hydrodynamically locked morphogenesis in karst and ice flutings. *J. Fluid Mech.* **778**, 89–119.
- CAMPOREALE, C., CANUTO, C. & RIDOLFI, L. 2012 A spectral approach for the stability analysis of turbulent open-channel flows over granular beds. *Theor. Comput. Fluid Dyn.* **26**, 51–80.
- CAMPOREALE, C., MANTELLI, E. & MANES, C. 2013 Interplay among unstable modes in films over permeable walls. *J. Fluid Mech.* **719**, 527–550.
- CAMPOREALE, C. & RIDOLFI, L. 2012 Ice ripple formation at large Reynolds numbers. *J. Fluid Mech.* **694**, 225–251.
- CANUTO, C., HUSSAINI, M.Y., QUARTERONI, A. & ZANG, TH.A. 2006 *Spectral Methods. Fundamentals in Single Domains*. Springer-Verlag Berlin Heidelberg.
- CARUSO, A, VESIPA, R, CAMPOREALE, C, RIDOLFI, L & SCHMID, P.J. 2016 River bedform inception by flow unsteadiness: A modal and nonmodal analysis. *Phys. Rev. E* **93**, 053110.
- COSSU, C. & HWANG, Y. 2017 Self-sustaining processes at all scales in wall-bounded turbulent shear flows. *Phil. Trans. R. Soc. A* **375**, 20160088.
- COSSU, C., PUJALS, G. & DEPARDON, S 2009 Optimal transient growth and very large-scale structures in turbulent boundary layers. *J. Fluid Mech.* **619**, 79–94.
- DEMUREN, A. O. & RODI, W. 1984 Calculation of turbulence-driven secondary motion in non-circular ducts. *J. Fluid Mech.* **140**, 189–222.

- DIMOTAKIS, P. E. & BROWN, G.L. 1976 The mixing layer at high Reynolds number: large-structure dynamics and entrainment. *J. Fluid Mech.* **78** (3), 535–560.
- DRAZIN, P. G. & REID, W.H. 2004 *Hydrodynamic Stability*. Cambridge University Press.
- DRESSLER, R. F. 1949 Mathematical solution of the problem of roll-waves in inclined open channels. *Commun. Pure Appl. Math.* **2**, 149–194.
- DUAN, Y., CHEN, Q., LI, D. & ZHONG, Q. 2020 Contributions of very large-scale motions to turbulence statistics in open channel flows. *J. Fluid Mech.* **892**, A3.
- DUAN, Y., ZHONG, Q., WANG, G., ZHANG, P. & LI, D. 2021 Contributions of different scales of turbulent motions to the mean wall-shear stress in open channel flows at low-to-moderate Reynolds numbers. *J. Fluid Mech.* **892**, A40.
- FINNIGAN, J. J., SHAW, R. H. & PATTON, E. G. 2009 Turbulence structure above a vegetation canopy. *J. Fluid Mech.* **424**, 637–387.
- GERARD, R. 1978 Secondary flow in noncircular conduits. *J. Hydr. Div. ASCE* **104** (5), 755–773.
- GESSNER, F. B. & JONES, J. B. 1965 On some aspects of fully-developed turbulent flow in rectangular channels. *J. Fluid Mech.* **23** (4), 689–713.
- DE GIOVANETTI, M., SUNG, H. J. & HWANG, Y. 2017 Streak instability in turbulent channel flow: the seeding mechanism of large-scale motions. *J. Fluid Mech.* **832**, 483–513.
- GOLUB, G. H. & VAN LOAN, C.F. 1996 *Matrix Computations*. Johns Hopkins University Press.
- HALL, P. 2018 Vortex/wave interaction arrays: a sustaining mechanism for the log layer? *J. Fluid Mech.* **850**, 46–82.
- HALL, P. & SMITH, F.T. 1988 The nonlinear interaction of Görtler vortices and Tollmien-Schlichting waves in curved channel flows. *Proc. R. Soc. Lond. A* **417**, 255–282.
- HALL, P. & SMITH, F. T. 1991 On strongly nonlinear vortex/wave interactions in boundary-layer transition. *J. Fluid Mech.* **227**, 641–666.
- HAMILTON, JAMES M., KIM, JOHN & WALEFFE, FABIAN 1995 Regeneration mechanisms of near-wall turbulence structures. *J. Fluid Mech.* **287**, 317–348.
- HO, C.-M., ZOHAR, Y., FOSS, J. K. & BUELL, J. C. 1991 Phase decorrelation of coherent structures in a free shear layer. *J. Fluid Mech.* **230**, 319–337.
- HURTHUR, D., LEMMIN, U. & TERRAY, E.A. 2007 Turbulent transport in the outer region of rough-wall open-channel flows: the contribution of large coherent shear stress structures (lc3s). *J. Fluid Mech.* **574**, 465–493.
- HWANG, Y & COSSU, C. 2010 Linear non-normal energy amplification of harmonic and stochastic forcing in the turbulent channel flow. *J. Fluid Mech.* **664**, 51–73.
- IKEDA, S. 1981 Self formed straight channels in sandy beds. *J. Hydraul. Div.-ASCE* **107** (4), 389–406.
- JIMENEZ, J & MOIN, P. 1991 The minimal flow unit in near-wall turbulence. *J. Fluid Mech.* **225**, 213–240.
- KIM, H., KLINE, S. & REYNOLDS, W. 1971 The production of turbulence near a smooth wall in a turbulent boundary layer. *J. Fluid Mech.* **50**, 133–160.
- KIM, K & ADRIAN, R. 1999 Very large-scale motion in the outer layer. *Phys. Fluids* **11**, 417–422.
- MARUSIC, I., MCKEON, B., MONKEWITZ, PETER, NAGIB, HASSAN, SMITS, ALEXANDER & SREENIVASAN, K. 2010 Wall-bounded turbulent flows at high Reynolds numbers: Recent advances and key issues. *Phys. Fluids* **22**, 065103.
- MCLEAN, S.R. 1981 The role of non-uniform roughness in the formation of sand ribbons. *Mar. Geol.* **42** (1), 49–74, sedimentary dynamics of continental shelves.
- NEZU, I & NAKAGAWA, H. 1984 Cellular secondary currents in straight conduit. *J. Hydraul. Eng.* **110** (2), 173–193.
- NEZU, I & NAKAGAWA, H. 1993 *Turbulence in open channel flows*. Balkema.
- NIKORA, V & ROY, A. 2012 *Secondary Flows in Rivers: Theoretical Framework, Recent Advances, and Current Challenges*, chap. 1, pp. 1–22. John Wiley & Sons, Ltd.
- PARK, J, HWANG, Y & COSSU, C. 2011 On the stability of large-scale streaks in turbulent Couette and Poiseuille flows. *Compt. Rend. Mec.* **339**, 1–5.
- PERKINS, H. J. 1970 The formation of streamwise vorticity in turbulent flow. *J. Fluid Mech.* **44** (4), 721–740.
- PERUZZI, C., POGGI, D., RIDOLFI, L. & MANES, C. 2020 On the scaling of large-scale structures in smooth-bed turbulent open-channel flows. *J. Fluid Mech.* **889**, A1.

- PUJALS, G., GARCIA-VILLALBA, M., COSSU, C. & DEPARDON, S. 2009 A note on optimal transient growth in turbulent channel flows. *Phys. Fluids* **21**.
- RASHIDI, M. & BANERJEE, S. 1988 Turbulence structure in free-surface channel flows. *Phys. Fluids* **31**.
- RAUPACH, M. R. & SHAW, R. H. 2009 Averaging procedures for flow within vegetation canopies. *Bound.-Layer Meteorol.* **22** (1), 79–90.
- ROY, A.G., BUFFIN-BÉLANGER, T., LAMARRE, H. & KIRKBRIDE, A.D. 2004 Size, shape and dynamics of large-scale turbulent flow structures in a gravel-bed river. *J. Fluid Mech.* **500**, 1–27.
- SCHMID, P. & HENNINGSON, D. 2001 *Stability and Transition in Shear Flows*, vol. 142. Springer.
- SHVIDCHENKO, A. & PENDER, G. 2001 Macroturbulent structure of open-channel flow over gravel beds. *Water Resour. Res.* **37**.
- TAMBURRINO, A. & GULLIVER, J. 2010 Large flow structures in a turbulent open channel flow. *J. Hydraul. Res.* **May 1999**, 363–380.
- TAN, W.Y. 1992 *Shallow Water Hydrodynamics*. Elsevier Science.
- TOWNSEND, A.A. 1976 *The structure of turbulent shear flow*. Cambridge University Press.
- WALEFFE, F. 1995 Hydrodynamic stability and turbulence: Beyond transients to a self-sustaining process. *Stud. Appl. Math.* **95** (3), 319–343.
- WALEFFE, F. 1997 On a self-sustaining process in shear flows. *Phys. Fluids* **9**, 883–900.
- WALEFFE, F. 2010 Exact coherent structures in channel flow. *J. Fluid Mech.* **435**, 93–102.
- WHITHAM, G.B. 1974 *Linear and Non Linear Waves*. John Wiley & Sons.
- ZAMPIRON, A., CAMERON, S. & NIKORA, V. 2020 Secondary currents and very-large-scale motions in open-channel flow over streamwise ridges. *J. Fluid Mech.* **887**, A17.
- ZHANG, P, DUAN, Y., LI, L, HU, J, LI, W. & YANG, S 2019 Turbulence statistics and very-large-scale motions in decelerating open-channel flow. *Phys. Fluids* **31**, 125106.